Global Lake Evaporation Estimates by Integrating Penman Method with Equilibrium Temperature Approach

UMAR FAROOQ,[a,b] HEPING LIU,[a] QIANYU ZHANG,[a] JINGFENG WANG,[c] AND LIAN SHEN[d]

[a] *Department of Civil and Environmental Engineering, Washington State University, Pullman, Washington*
[b] *CSIRO Agriculture and Food, Black Mountain, Australian Capital Territory, Australia*
[c] *School of Civil and Environmental Engineering, Georgia Institute of Technology, Atlanta, Georgia*
[d] *Department of Mechanical Engineering and St. Anthony Falls Laboratory, University of Minnesota, Minneapolis, Minnesota*

(Manuscript received 31 October 2024, in final form 2 June 2025, accepted 19 July 2025)

ABSTRACT: Modeling evaporation E from inland water bodies is challenging largely due to the uncertainties of input data, particularly surface water temperature that plays a key role in the available energy, i.e., net radiation R_n minus rate of water heat storage change G. The equilibrium temperature approach (ETA) for estimating water surface temperature offers an alternative method to calculate R_n and G using standard meteorological data. This study evaluates the global lake E estimates from the widely used Penman model (PM) coupled with the ETA (PM-ETA) against field observations and model simulations from the Lake, Ice, Snow, and Sediment Simulator (LISSS). Our analysis reveals that the PM-ETA tends to overestimate E by approximately 36% and 24% compared to observations and the LISSS simulations, respectively, despite being driven by the same input data. The biases of the PM-ETA E are more pronounced in the cold and polar regions with distinct seasonality of R_n and G. Furthermore, the E trends from the PM-ETA deviate from the LISSS simulations over the period of 2001–16 due to the bias trends in the available energy. By incorporating the LISSS-simulated R_n and G into the PM, the bias in E is reduced to less than ±5% compared to the LISSS results. This study highlights the need to improve the available energy input of the PM to improve the estimates of global lake E for better water resource management and planning.

SIGNIFICANCE STATEMENT: This study addresses a crucial challenge in modeling evaporation E from inland water bodies—uncertainties in surface water temperature and available energy inputs, particularly net radiation R_n and rate of heat storage change G. By evaluating the widely used Penman model (PM) coupled with the equilibrium temperature approach (ETA), we reveal a tendency for the PM-ETA to overestimate E globally, with the largest biases observed in cold and polar regions. Incorporating higher-quality R_n and G estimates from the Lake, Ice, Snow, and Sediment Simulator (LISSS) significantly reduces these biases. These findings highlight the importance of alternative higher-quality data products for available energy inputs for improving E estimates by the PM.

KEYWORDS: Energy budget/balance; Evaporation; Hydrometeorology; Freshwater; Water resources

1. Introduction

Inland waters, covering 4.2 million km^2 (Downing et al. 2006), are vital freshwater sources (Prigent et al. 2012). At present, four billion people worldwide face severe water scarcity (Mekonnen and Hoekstra 2016), which makes the sustainable use of freshwater resources imperative for global food security and development (Kummu et al. 2016; Muzammil et al. 2023). Evaporation E represents a major loss of freshwater, making its accurate estimation pivotal for water resource management (La Fuente et al. 2024; Prigent et al. 2012; Tian et al. 2022). However, the estimates of lake E through process-based models, particularly at the global scale, are subject to substantial uncertainties due to the lack of adequate input data for these models.

Three groups of process-based models have been developed to estimate lake E: aerodynamic models (Harbeck et al. 1958; Pasquill 1943), energy balance models (Bowen 1926), and combination models (Penman 1948; Priestley and Taylor 1972). In all these models, surface water temperature T_s is required to calculate the vertical vapor pressure difference ($e_D = e_s - e_a$) between vapor pressure at the water surface e_s and near-surface vapor pressure e_a, net radiation R_n, and rate of heat storage change of water body G. Historically, direct measurements of T_s for modeling longwave radiation from the water surface have been rare, particularly at global scales. Hence, empirical equations are used to calculate R_n from standard meteorological data including air temperature (McMahon et al. 2013), while G is often neglected in such estimations (Penman 1948). On daily or longer time scales, the available energy ($R_n - G$) dominates the variations in E (Gan and Liu 2020; Lenters et al. 2005; Shao et al. 2020), underscoring the crucial role of G in estimating E.

Modeling approaches for estimating T_s are categorized into two broad groups: statistical models and deterministic models (Caissie 2006). Statistical models, such as linear regression models, nonlinear regression models, and stochastic regression

Supplemental information related to this paper is available at the Journals Online website: https://doi.org/10.1175/JHM-D-24-0146.1.s1.

Corresponding author: Heping Liu, heping.liu@wsu.edu

DOI: 10.1175/JHM-D-24-0146.1

models, use regression techniques to correlate T_s with air temperature (Benyahya et al. 2007). Since T_s is also influenced by solar radiation, wind speed, and water body depth, the statistical models are not a reliable tool to estimate T_s (Ficklin et al. 2012). Deterministic models estimate T_s using the surface energy balance (i.e., heat fluxes) (Benyahya et al. 2007; Hebert et al. 2011). The heat fluxes calculated at the air–water interface require incoming and reflected shortwave radiation, incoming and outgoing longwave radiation, evaporative heat loss, and heat transfer in the water body. However, the unavailability of some of these variables limits the application of deterministic models, particularly on a global scale.

To address this issue, the equilibrium temperature approach (ETA) was developed to estimate T_s based on standard meteorological data (Edinger et al. 1968). This method combines all heat flux terms in the deterministic models assuming zero net heat exchange between the water surface and air when the well-mixed water body reaches equilibrium temperature T_e. Although water bodies tend to reach T_e, actual T_s always lags T_e by a certain amount, known as the time constant (τ). Thereby, T_s expressed as a function of T_e, τ, and water body depth is used to estimate G. Similar approaches have been employed by Keijman (1974), Fraedrich et al. (1977), and de Bruin (1982) to estimate G as a function of T_s using standard meteorological variables. A brief description of the ETA (Edinger et al. 1968) is provided in section 2b. Despite relying solely on the ETA to estimate G from standard meteorological data, several studies have reported its good performance (Bai and Wang 2023; Du et al. 2022, 2018; Zhu et al. 2019). Nevertheless, water bodies are not always well mixed and thus have a depth-dependent temperature profile with the exchange heat with sediments/bedrocks, leading to variations in T_s and consequently E (Stepanenko et al. 2013).

Another class of approaches for estimating lake E includes lake models such as the Lake, Ice, Snow, and Sediment Simulator (LISSS), which is part of the Community Land Model (CLM) (Oleson et al. 2013). The LISSS simulates E, T_s, R_n, and G for water bodies as well as the lake water temperature profile considering heat exchange between water and sediments/bedrocks (section 2c). The LISSS provides a unique opportunity to quantify the impacts of biases in R_n and G on the uncertainties of estimated E. In this study, we evaluate E estimates using the Penman method (PM) coupled with the ETA, referred to as the PM-ETA E hereafter, against observations and the LISSS-simulated E. Despite the increasing availability of remotely sensed T_s data of inland water bodies (Korver et al. 2024; Layden et al. 2015; Lieberherr and Wunderle 2018), we used the ETA alongside the PM in this study. This decision was driven by the historical significance and widespread application of the ETA in open water E research, as well as its convenience for estimating R_n and G using widely available meteorological data (McMahon et al. 2013; Piccolroaz et al. 2024). Although both remote sensing and ETA have advantages, the latter remains a preferred tool for long-term and large-scale E studies, particularly where high-frequency satellite data are unavailable or incomplete.

In this study, we demonstrate that the PM's performance in simulating E is substantially improved when the improved simulations of R_n and G from the LISSS are used in the PM. The PM is selected for three reasons: superior performance to other process-based methods such as Priestley–Taylor (Stewart and Rouse 1976), de Bruin–Keijman (1979), Brutsaert–Stricker (Brutsaert and Stricker 1979), and mass transfer (Harbeck et al. 1958); explicit representation of standard meteorological variables such as air temperature, solar radiation, humidity, and wind speed in the PM formulation (section 2b); and being widely used in the analysis of long-term E trends and its environmental drivers (Cui et al. 2021; Guan et al. 2022; Roderick et al. 2007; Xie et al. 2015; You et al. 2013; Zhou et al. 2021). This study aims to (i) assess the E estimates by the PM coupled with the ETA in capturing spatial and temporal variations in global lake E and (ii) examine the bias reduction of the PM E by using the LISSS simulations of R_n and G.

2. Methods

a. Forcing data and simulation setup

Global lake E is simulated using both the PM-ETA and the LISSS for the period spanning from 2001 to 2016 driven by CRUNCEP atmospheric forcing data, which combines high-quality climate data from the Climatic Research Unit (CRU) with atmospheric reanalysis data from the National Centers for Environmental Prediction (NCEP). Geographic locations and morphometric attributes, such as altitude, surface area, and lake depth, are obtained from the LISSS in the CLM (CLM/LISSS), version 4.5. The CLM/LISSS uses the Global Lake and Wetland Database (Lehner and Döll 2004) and the Global Gridded Dataset of Lake Coverage and Lake Depth for Numerical Weather Prediction and Climate Modeling (Kourzeneva et al. 2012) to define global water bodies. The PM-ETA E is calculated at a monthly time scale, while the LISSS simulates half-hourly surface energy fluxes aggregated to a monthly time scale for comparison purposes. In addition to using the ETA, the PM E driven by R_n and G from the LISSS outputs, referred to as PM-LISSS E hereafter, is also assessed in comparison with the PM-ETA and LISSS E. We emphasize that PM-LISSS is not intended as a stand-alone E method but rather as a diagnostic sensitivity experiment to isolate the role of R_n and G biases in driving PM-ETA errors. Since the complete descriptions of the PM and the LISSS are documented elsewhere (Penman 1948; Oleson et al. 2013; Subin et al. 2012b), only brief descriptions are provided in sections 2b and 2c, respectively.

This study primarily focuses on evaluating the performance of the PM-ETA in estimating spatial and temporal variations in global lake E against the LISSS-derived E when driven by the same forcing dataset (i.e., CRUNCEP). While a comprehensive uncertainty analysis involving multiple forcing datasets is beyond the scope of this study, we included a targeted comparison between the CRUNCEP forcing data and the Princeton Global Forcing Dataset (Sheffield et al. 2006) in section 2d to illustrate the potential influence of forcing data on E estimates.

b. The Penman-Equilibrium temperature approach (PM-ETA)

The PM E (mm day^{-1}) is expressed as

$$E = \frac{s(R_n - G) + \gamma \lambda f_{(u)}(e_s - e_a)}{\lambda(s + \gamma)}, \quad (1)$$

where s (kPa °C^{-1}) is the slope of saturation vapor pressure, R_n (MJ m^{-2} day^{-1}) is the net radiation, G (MJ m^{-2} day^{-1}) is the rate of change in water heat storage, γ (kPa °C^{-1}) is the psychrometric constant, $f_{(u)}$ (MJ m^{-2} day^{-1} kPa °C^{-1}) is the wind function, e_s (kPa) is the saturation vapor pressure at air temperature, e_a (kPa) is the actual vapor pressure, and λ (MJ kg^{-1}) is the latent heat of vaporization. While there are several aerodynamic functions available to estimate $f_{(u)}$, we adopted an area-dependent aerodynamic function that has demonstrated efficacy in estimating evaporation from water bodies with diverse morphometric attributes (McJannet et al. 2012),

$$f_{(u)} = (2.33 + 1.65\,u)L_f^{-0.1}, \quad (2)$$

where u (m s^{-1}) is the wind speed at 2-m height and L_f is the fetch of water body. The L_f for each lake is obtained from the LISSS simulations. The estimation of R_n and G in Eq. (1) requires T_s, which is calculated using the equilibrium temperature and associated time constant (τ) approach. For a well-mixed water body, τ and T_s are calculated as (Finch and Hall 2001)

$$\tau = \frac{\rho_w c\, d}{4\sigma(T_n + 273.15)^3 + f_{(u)}(s_n + \gamma)}, \quad (3)$$

$$T_e = T_n + \frac{R_n^*}{4\sigma(T_n + 273.15)^3 + f_{(u)}(s_n + \gamma)}, \quad (4)$$

where ρ_w (kg m^{-3}) is the density of water, c (MJ kg^{-1} °C^{-1}) is the specific heat of water, d (m) is the depth of water body, σ (MJ m^{-2} K^{-4} day^{-1}) is the Stefan–Boltzmann constant, T_n (°C) is the wet-bulb temperature, s_n (kPa °C^{-1}) is the slope of saturation vapor pressure curve at T_n, and R_n^* (MJ m^{-2} day^{-1}) is the net radiation if the water surface is at T_n. The R_n^* is calculated following the Finch and Hall (2001), considering the emissivity of water and cloudiness factor. A detailed description of R_n^* calculation is given in Text S1 in the online supplemental material. After calculating the T_e, T_s is calculated as

$$T_{s,i} = T_e + (T_{s,i-1} - T_e)e^{-dt/\tau}, \quad (5)$$

where $T_{s,i}$ (°C) is the temperature of water body at the current time step, $T_{s,i-1}$ (°C) is the temperature of water body at the previous time step, and dt (number of days) is the time step. The G in Eq. (S1) is calculated as (Finch and Hall 2001)

$$G = \rho_w c\, d\frac{T_{s,i} - T_{s,i-1}}{dt}, \quad (6)$$

and the R_n is

$$R_n = (1 - \alpha)K_\downarrow + L_\downarrow - f_c\,\sigma\,\varepsilon_w[(T_a + 273.15)^4 + 4(T_a + 273.15)^3(T_{s,i-1} - T_a)]. \quad (7)$$

c. The LISSS model

The LISSS is a 1D model to simulate surface energy fluxes from water bodies at subgrid scale within the CLM, which uses a nested hierarchy of five land units (glacier, urban, agriculture, vegetation, and lake) to represent the land surface heterogeneity (Oleson et al. 2013; Subin et al. 2012b). The CLM combines all lakes within a grid cell by using the mean depth and runs LISSS at the subgrid level as one tile to calculate water surface energy fluxes. The LISSS incorporates the effect of snow/ice phenology and sediment heat exchange on surface energy fluxes by unifying each lake as a snow–lake–soil system. Lake physics includes phase change of ice and snow and heat mixing caused by convection and wind-driven eddies (Hostetler and Bartlein 1990), molecular diffusion, 3D circulations, and buoyant convection (Fang and Stefan 1996a). The model discretizes each lake vertically into 0–5 snow layers, 10 water and ice layers, and 15 soil and bedrock layers and implements the lake (water body) energy balance:

$$\varphi S + L_\downarrow - L_\uparrow = \mathrm{LE} + H + G, \quad (8)$$

where S (W m^{-2}) is the total absorbed shortwave radiation in lake, φ is the fraction of S absorbed at lake surface, LE (W m^{-2}) is the latent heat flux, H (W m^{-2}) is the sensible heat flux, and G (W m^{-2}) is the rate of heat storage of water body. The LE is

$$\mathrm{LE} = \lambda\,\rho_a\frac{q_s - q_a}{r_{aw}}, \quad (9)$$

where λ (J kg^{-1}) is the latent heat of vaporization, ρ_a (kg m^{-3}) is the air density, q_s (kg kg^{-1}) is the saturated specific humidity at T_s, q_a (kg kg^{-1}) is the specific humidity of air, and r_{aw} (s m^{-1}) is the aerodynamic resistance to water vapor transfer. The H is given as

$$H = \rho_a C_p\frac{\theta_a - T_s}{r_{ah}}, \quad (10)$$

where C_p (J kg^{-1} K^{-1}) is the specific heat capacity of air, θ_a (K) is the air potential temperature, and r_{ah} (s m^{-1}) is the aerodynamic resistance to heat transfer. Monin–Obukhov similarity theory is used to calculate r_{aw} and r_{ah} as a function of wind speed and atmospheric stability. The G is calculated as follows:

$$G = \frac{2\kappa_T}{z_T}(T_s - T_T), \quad (11)$$

where κ_T (W m^{-1} K^{-1}) is the thermal conductivity, T_T (K) is the temperature of top layer, and z_T (m) is the thickness of top layer. For ice-free lakes in global simulations, z_T is 0.1 m.

TABLE 1. Evaluation of simulated evaporation against observations. The mean monthly evaporation rate is simulated by the PM-ETA, LISSS, and PM-LISSS.

Name	Location	Observation duration	r^2			RMSE (mm day^{-1})			MBE (%)			Reference
			PM-ETA	LISSS	PM-LISSS	PM-ETA	LISSS	PM-LISSS	PM-ETA	LISSS	PM-LISSS	
Lake Taihu	31.2°N, 120.1°E	June 2010–May 2011	0.30	0.61	0.63	1.9	1.4	1.5	71.7	54.4	59.4	Zhang et al. (2020)
Ross Barnett	32.0°N, 90.0°W	January 2008–December 2008	0.59	0.87	0.89	1.2	0.6	0.6	21.0	8.3	9.7	Liu et al. (2012)
Lake Mohave	35.2°N, 114°W	January 2014–December 2014	0.88	0.84	0.80	1.1	2.0	1.8	−19.3	−36.4	−32.2	Moreo (2015)
Lake Mead	36.0°N, 114.0°W	January 2014–December 2014	0.67	0.66	0.64	1.3	1.0	1.0	12.8	−9.8	−1.4	Moreo (2015)
Lake Suwa	36.0°N, 138.1°E	January 2016–December 2016	0.14	0.51	0.52	1.2	0.7	0.7	12.5	−1.4	3.1	Pastorello et al. (2020)
Eastmain	52.1°N, 75.9°W	January 2011–December 2011	0.84	0.77	0.71	1.2	0.8	0.9	12.8	−0.3	1.6	Pastorello et al. (2020)
Lake Dagowsee	53.2°N, 13.0°E	June 2015–May 2016	0.66	0.86	0.88	1.2	0.7	0.7	54.9	29.7	34.0	Pastorello et al. (2020)
Lake Tamnaren	60.2°N, 17.3°E	March 2011–December 2011	0.27	0.48	0.49	1.9	1.4	1.4	141.4	106.3	104.9	Pastorello et al. (2020)
Lake Vanajavesi	61.1°N, 24.3°E	January 2016–December 2016	0.71	0.94	0.94	1.0	0.4	0.4	16.3	−9.7	−9.5	Pastorello et al. (2020)
Average			0.56	0.73	0.72	1.3	1.0	1.0	36.0	15.7	−9.5	

The $L_{\uparrow}$ is estimated using the Stefan–Boltzmann law. Both the surface energy and momentum fluxes depend implicitly on T_s; therefore, LE, H, G, $L_{\downarrow}$, and $L_{\uparrow}$ are calculated simultaneously using the Newton–Raphson method as follows:

$$dT_s = \frac{\varphi S + L_{\downarrow} - L_{\uparrow} - LE - H - G}{\frac{\partial L_{\downarrow}}{\partial T_s} + \frac{\partial L_{\uparrow}}{\partial T_s} + \frac{\partial LE}{\partial T_s} + \frac{\partial H}{\partial T_s} + \frac{\partial G}{\partial T_s}}, \tag{12}$$

where dT_s is the temperature difference between the previous and current time steps and $\partial/\partial T_s$ is the partial derivation of respective surface energy flux with respect to T_s. The LISSS performs four iterations to get a converged solution of Eq. (12). The LISSS simulations are conducted from 2001 to 2016, as driven by the CRUNCEP atmospheric forcing data at 30-min intervals after 50 years of spin-up. The outputs from the lake tiles are used in the offline analysis to determine spatiotemporal variabilities in global lake E.

d. Validation of forcing dataset

The uncertainties of the forcing data contribute to the biases of the modeled lake E. We evaluated the accuracy of the CRUNCEP forcing data against in situ observations and the Princeton University forcing data (Sheffield et al. 2006). The CRUNCEP air temperature, R_n, and relative humidity demonstrate good agreement with observations (Figs. S1–S3). However, wind speed data show a considerable bias (Fig. S4). On the time scale larger than daily, however, previous studies have shown that wind speed plays a minor role in E variability compared to the energy balance (Blanken et al. 2000; Farooq et al. 2022; Hostetler and Bartlein 1990; Liu et al. 2012; Xiao et al. 2018). Our tests further demonstrate that lake E has low sensitivity to wind speed variability on monthly time scales (Fig. S5). Therefore, the contribution of wind speed to the overall uncertainty of the modeled lake E is likely to be small. Furthermore, the two sets of E simulated by the LISSS using the CRUNCEP and the Princeton University forcing data show a high correlation ($r^2 = 0.99, p < 0.01$) and minimal bias [absolute error (AE) = 0.24 mm day^{-1}, mean bias error (MBE) = 12.3%] (Fig. S6). Considering the fact that the CRUNCEP is a widely used data product consistent with the Princeton University forcing dataset, we have chosen to utilize the CRUNCEP dataset for subsequent analysis.

e. Data analysis methods

The PM-ETA E is evaluated against the LISSS E during the ice-free season (summer and autumn). Spatial comparisons between PM-ETA and LISSS E are performed for the year 2016, while the evaluation of the temporal variations of PM-ETA E is performed for the period of 2001–16. The temporal variability in E is quantified using Theil–Sen's linear regression, a robust nonparametric method that calculates all possible slopes between data points and returns the median slope as the estimate of the linear trend (Sen 1968). The PM-ETA E evaluation is performed on a global scale as well as for five climate regions: tropical, arid, temperate, cold, and polar, based on the Köppen–Geiger climate classification

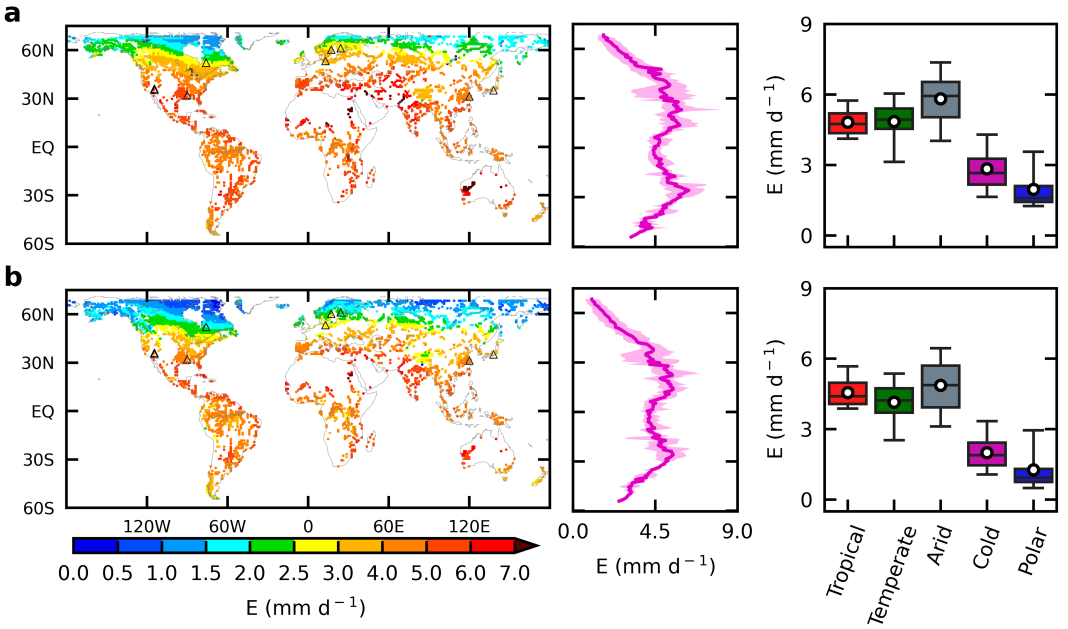

FIG. 1. Spatial distribution of the mean E during 2001–16 with open water. (a) PM-ETA E. (b) LISSS E. Each row, from left to right, shows the spatial distribution of E, zonal-mean E, and the mean E in the five climate regions. Black-outlined hollow triangles indicate the locations of lakes with available observed data used for validation and analysis (Table 1). The shaded areas in the zonal-mean plots represent the 10th and 90th percentiles of E. The boxes in the right panels represent the 25th, 50th, and 75th percentiles of E. The lower and upper whiskers show the 5th and 95th percentiles of E, respectively. The mean E in each climate region is shown by a white dot.

(Fig. S7) (Beck et al. 2018). Note that the seasons are synchronized for both the Northern and Southern Hemispheres. The summer is defined as June–August for the Northern Hemisphere and December–February for the Southern Hemisphere, while autumn is defined as September–November for the Northern Hemisphere and March–May for the Southern Hemisphere.

3. Results and discussion

a. *Comparison of PM-ETA and LISSS E with observations*

The LISSS has been used in previous studies to estimate lake E validated against observations (e.g., Hu et al. 2017; Subin et al. 2012b; Wang et al. 2018; Xiao et al. 2018; Zhou et al. 2021). The validation of LISSS-simulated lake E and T_s against observations (Farooq et al. 2022) shows good agreement with $r^2 = 0.89$, root-mean-square error (RMSE) = 12.02 W m^{-2}, and $p < 0.01$ for E and $r^2 = 0.96$, RMSE = 1.8°C, and $p < 0.01$ for T_s. Nevertheless, in this study, we simultaneously evaluated the PM-ETA and LISSS E against observations (Table 1, Fig. S8). The selected water bodies for evaluation have a diverse range of morphometric attributes across regions to ensure representativeness. Our analysis shows that the LISSS performs better than the PM-ETA in simulating E. The mean r^2 between the PM-ETA E (LISSS E) and the observations is 0.56 (0.73) with a range of 0.14–0.88 (0.48–0.94) across the water bodies. The average RMSE of PM-ETA E (1.3 mm day^{-1}) is 33% higher than that of the LISSS E (1.0 mm day^{-1}), with PM-ETA RMSE values ranging from 1.0 to 1.9 mm day^{-1}. The systematic bias (i.e., MBE) of the PM-ETA E (36.0%) is more than double that of the LISSS E (16%), varying from −19% to 141% (Table 1). The model performance varies substantially across lakes, and this disparity stems from a complex interplay between background climate, model structure, forcing data quality, and lake morphometry.

In arid regions, where radiation dominates the E process, the PM-ETA tends to outperform the LISSS (e.g., RMSE = 1.1 mm day^{-1} at Lake Mohave vs 2.0 mm day^{-1} for LISSS). This is partly because the PM-ETA, operating at a monthly time step, effectively emphasizes radiation-driven processes, which dominate E in hot, dry environments. Additionally, in such climates, humidity gradients are large but relatively stable, making the PM-ETA less sensitive to biases in relative humidity (RH) (Fig. S3). In contrast, the LISSS, simulated at a 30-min resolution, is more sensitive to short-term variations in near-surface atmospheric conditions. When coupled with known biases in the forcing data, i.e., underestimation of T_a (RMSE = 3.2°–7.0°C) and overestimation of RH (RMSE = 9.9%), this sensitivity contributes to the LISSS's underperformance in these arid settings (Figs. S1 and S3). Conversely, in temperate and cold climate lakes, the LISSS shows better agreement with observations. These lakes typically experience strong diurnal and seasonal stratification, significant sediment heat flux, and seasonal ice-related dynamics, all of which are better captured by the LISSS's process-based energy balance approach. For instance, in the temperate region, the LISSS outperforms the PM-ETA at shallow lakes by resolving rapid shifts in surface

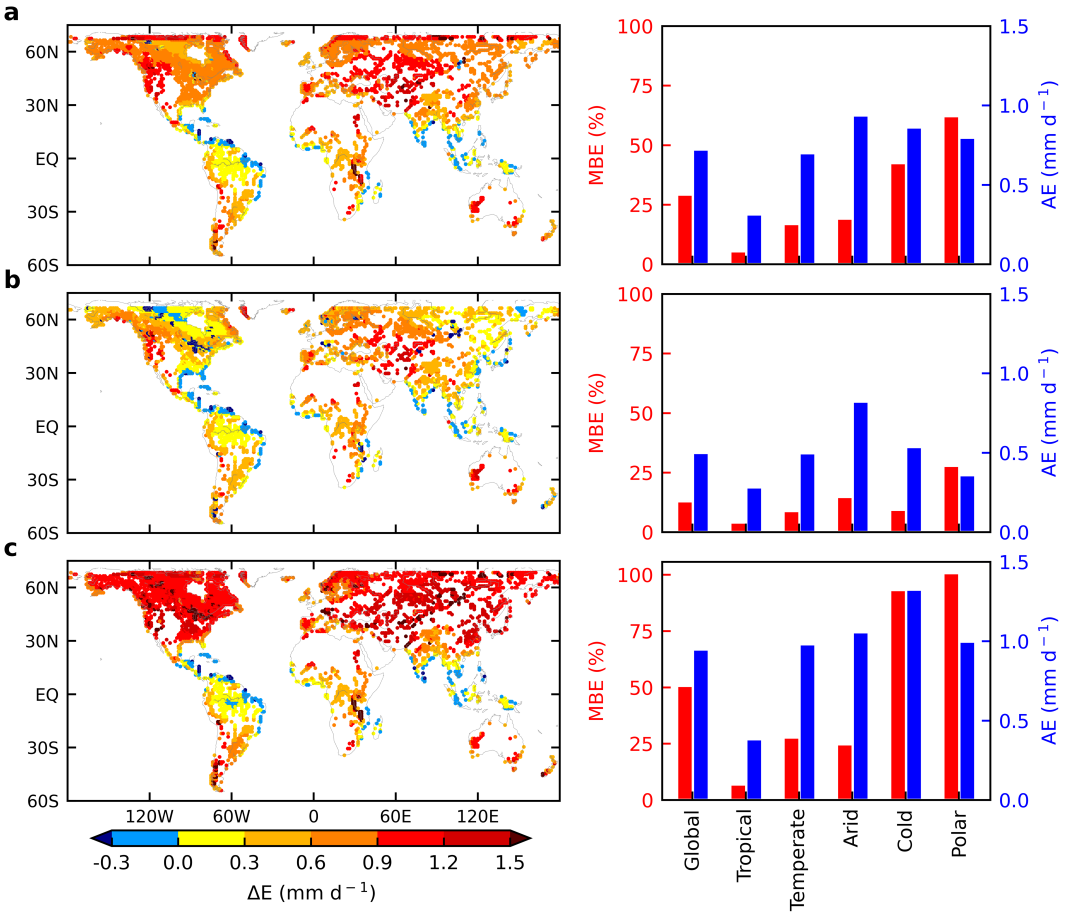

FIG. 2. Evaluating PM-ETA E against LISSS. (a) Entire period with open water. (b) Summer. (c) Autumn. (left) The spatial distribution of E difference in the PM-ETA and LISSS estimates, where positive values denote higher PM-ETA E. (right) The MBE and AE on a global scale and in the five climate regions.

heat storage and vapor gradients, while the PM-ETA, which assumes a well-mixed water column and lacks representation of sediment fluxes, tends to overestimate E (e.g., MBE = 71.7% for Lake Taihu). In high-latitude lakes, the LISSS captures residual heat release and delayed ice melt effects, mitigating errors even in the presence of forcing biases (e.g., underestimated T_a and overestimated RH), whereas the PM-ETA substantially overestimates E (e.g., MBE = 141.4% for Lake Tamnaren). Although no single factor consistently explains the variation, the interaction among climate regime, forcing quality, and lake-specific physical processes largely determines model accuracy. Despite some regional biases, LISSS consistently outperforms PM-ETA in most observational comparisons, particularly in stratified and humid lakes, and is thus selected as a physically based reference model in this study to enable more mechanistic insights into PM-ETA's limitations across space and time.

b. Spatial variability in PM-ETA E versus LISSS E

The spatial distribution of the PM-ETA and LISSS E is shown in Fig. 1. The global-mean PM-ETA E (LISSS E) is 3.7 mm day^{-1} (3.0 mm day^{-1}), ranging from 0.03 (0.01 mm day^{-1}) to 23.9 mm day^{-1} (7.2 mm day^{-1}). Both models show two peaks in zonal-mean E around 15°N and 25°S with E decreasing toward polar regions. These latitudinal variations in the zonal-mean E are consistent with the latitudinal variations of R_n (Farooq et al. 2022). The largest lake E is observed in the arid region where PM-ETA E (LISSS E) is about 60% (66%) higher than the global-mean E. The polar and cold climate regions experience the lowest E during the ice-free period (Fig. 1).

The global-mean PM-ETA E surpasses the LISSS E by about 29% (Fig. 2a). The PM-ETA significantly overestimates E across all the climate regions except for the tropical region where the PM-ETA E agrees well with the LISSS E (MBE = 5% and AE = 0.31 mm day^{-1}). In contrast, relative to the LISSS, the PM-ETA overestimates E by 17%, 19%, 43%, and 62% in the temperate, arid, cold, and polar regions, respectively (Fig. 2a). The mean summertime PM-ETA E for the tropical, temperate, arid, cold, and polar regions exceeds the LISSS E by 4%, 9%, 15%, 9%, and 28%, respectively. In autumn, however, the bias in the global-mean PM-ETA E is 4.4 times higher than that during summer, accounting for 61% of the annual-mean bias (Figs. 2b,c). Except for the tropical region with a small change, a large increase in MBE is observed for

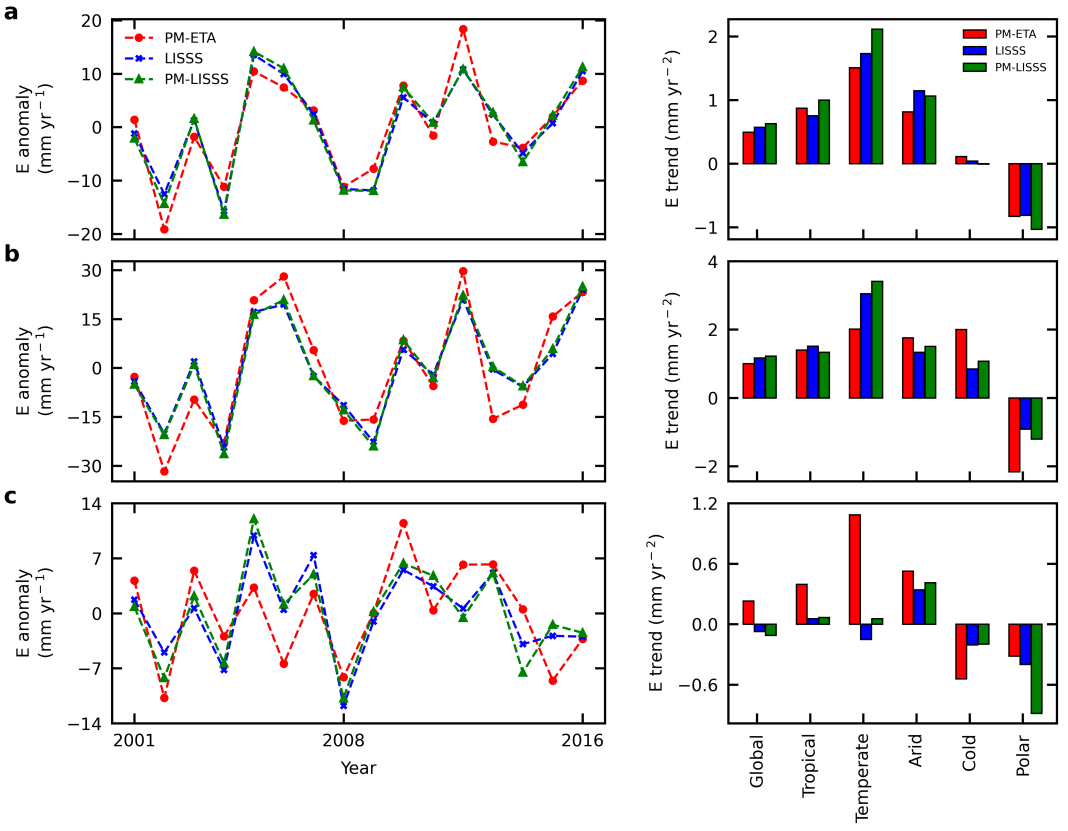

FIG. 3. Temporal variations in the PM-ETA E, LISSS E, and PM-LISSS E. (a) Entire period with open water. (b) Summer. (c) Autumn. (left) The time series of E anomalies. (right) The global E trends and the E trends in the five climate regions are shown.

all other regions during autumn (Fig. 2c). These large biases in spatial heterogeneity of PM-ETA E across seasons suggest large biases in the PM-ETA E trends compared to the LISSS E, as discussed in the following section.

c. *Temporal variability of PM-ETA E versus LISSS E*

The trends of the PM-ETA and LISSS E from 2001 to 2016 are shown in Fig. 3. The observed E datasets listed in Table 1 span less than 12 months and therefore do not support a robust trend analysis. Thus, the PM-ETA and LISSS E trends are not compared against observations. During ice-free periods, the PM-ETA E has a high correlation with the LISSS E ($r^2 = 0.85$, $p < 0.05$). The trend of the global-mean PM-ETA E (0.49 mm yr^{-2}) is 14% lower than that of the LISSS (0.57 mm yr^{-2}) (Fig. 3a). Both models demonstrate the maximum E trend in the temperate region with close agreement between the E ($r^2 = 0.94, p < 0.05$, MBE $= -13\%$). The lowest correlation between the PM-ETA and LISSS E occurs in the polar region ($r^2 = 0.75$, $p < 0.05$, MBE $= 3\%$). The PM-ETA E trends of the tropical, arid, and cold regions differ from the LISSS E trends by -16% ($r^2 = 0.84$, $p < 0.05$), 30% ($r^2 = 0.80$, $p < 0.05$), and 168% ($r^2 = 0.94$, $p < 0.05$), respectively. It is important to emphasize that the lake-wise E trends from both models exhibit significant spatial variability, with stronger trends during summer, particularly at mid–high latitudes (Fig. S9).

The PM-ETA E trends deviate from the LISSS E trends for all the regions in both summer and autumn (Figs. 3b,c). The PM-ETA performs the best in the tropical region in summer where the trends differ by 7% ($r^2 = 0.66$, $p > 0.05$) followed by the arid region. Despite a strong correlation between the two time series for the temperate ($r^2 = 0.88$, $p < 0.05$) and cold ($r^2 = 0.93$, $p < 0.05$) regions, the E trends differ significantly. For the polar region, the agreement is the lowest between the PM-ETA and LISSS E trends. Although the correlation is high during autumn (0.63–0.83), the PM-ETA E trends exhibit a large bias for all the regions (Fig. 3c). The larger bias in the PM-ETA E trends in autumn is consistent with the higher corresponding bias of the PM-ETA E. Previous studies indicated that the bias of process-based E estimates against observations is primarily attributed to the uncertainty of R_n and G calculated using empirical equations (Finch and Hall 2001; Hamdani et al. 2018). Furthermore, our analysis shows that the overall contribution of the radiative term to accumulated PM-ETA E is approximately 82%, while the aerodynamic term accounts for the remaining 18% (Fig. S10). Given that radiation is the major driver of E at monthly time scale, we focused on reducing the uncertainties of radiative forcing. Further improvement of E estimates may be achieved by improving the

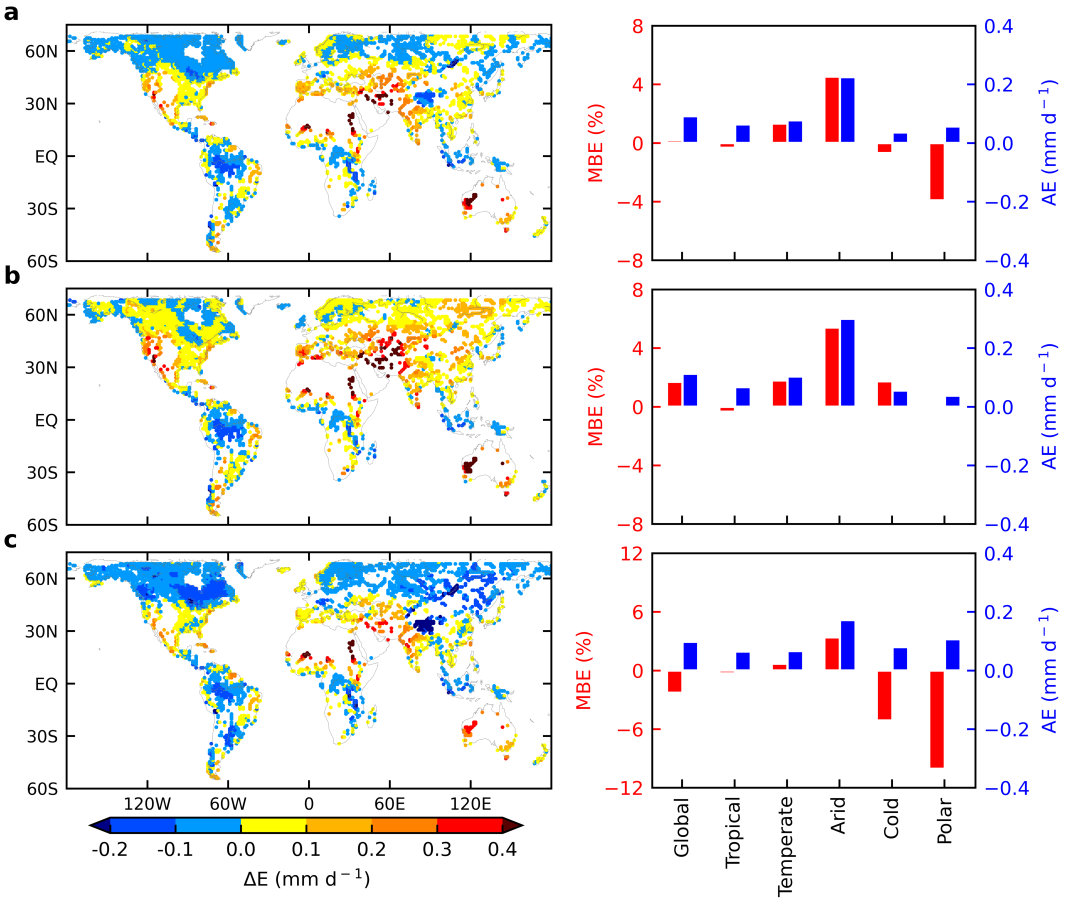

FIG. 4. Comparison of the PM-LISSS E with the LISSS E. (a) Entire period with open water. (b) Summer. (c) Autumn. (left) The spatial variability in difference between the PM-LISSS E and the LISSS E. (right) The MBE and AE on the global E and E in the five climate regions. The positive values represent the higher PM-LISSS E than the LISSS E.

parameterization of the transfer coefficient in the bulk flux formula, but this is beyond the scope of this study. The validation of R_n simulated by the LISSS and ETA against observations (Fig. S11, Table S1) shows the superior performance of LISSS in simulating R_n. Therefore, we will investigate whether replacing R_n and G in the PM with those simulated by the LISSS improves the performance of the PM in simulating E (i.e., PM-LISSS E) in the next section.

d. *Spatiotemporal variability in the PM-LISSS E in comparison with LISSS E*

Using $(R_n - G)$ simulated by the LISSS in the PM, the global-mean PM-LISSS E is almost equal to the global-mean LISSS E, with MBE within ±5% for all study regions (Fig. 4a). The PM-LISSS E has small positive biases in summer and small negative biases in autumn (Figs. 4b,c). Positive summer biases mostly occur in the temperate, arid, and cold regions, whereas negative autumn biases are observed in the cold and polar climate regions. The e_D and E exhibit weak (strong) correlation in summer (autumn) due to the effect of turbulent mixing (i.e., wind speed), particularly in mid- and high latitudes (Farooq et al. 2022). Since e_D is generally higher than the atmospheric vapor pressure deficit over water bodies, the weak (strong) relation between e_D and E leads to lower (higher) LISSS E in summer (autumn), compared to the PM-ETA E at mid- and high latitudes (Farooq et al. 2022).

The PM-LISSS E shows a strong correlation ($r^2 > 0.98$, $p < 0.01$) with the LISSS E during the ice-free periods (Fig. 3). The global-mean difference in the PM-LISSS and LISSS E trends is 0.05 mm yr^{-2}, ranging from −0.21 to 0.38 mm yr^{-2}. The difference in the PM-LISSS and LISSS E trends increases slightly for the tropical, arid, and polar regions compared to the PM-ETA and LISSS E trends (Fig. 3a). At seasonal time scales, the PM-LISSS E trends are consistent with the LISSS E trends for all the regions except for the polar region (Figs. 3b,c). Negative biases of the PM-LISSS E during autumn cause higher biases for the polar region. The overall improvement in PM-LISSS E indicates that the biases in R_n and G are closely related to the biases in PM-ETA E.

The validation against observed lake E verifies the improvement of the PM-LISSS E characterized by the mean r^2 between the PM-LISSS and observed E increases by 29% from 0.56 to 0.72, and the RMSE and MBE decrease by 33% and 48%, respectively (Table 1, Fig. S8). In addition, the statistics

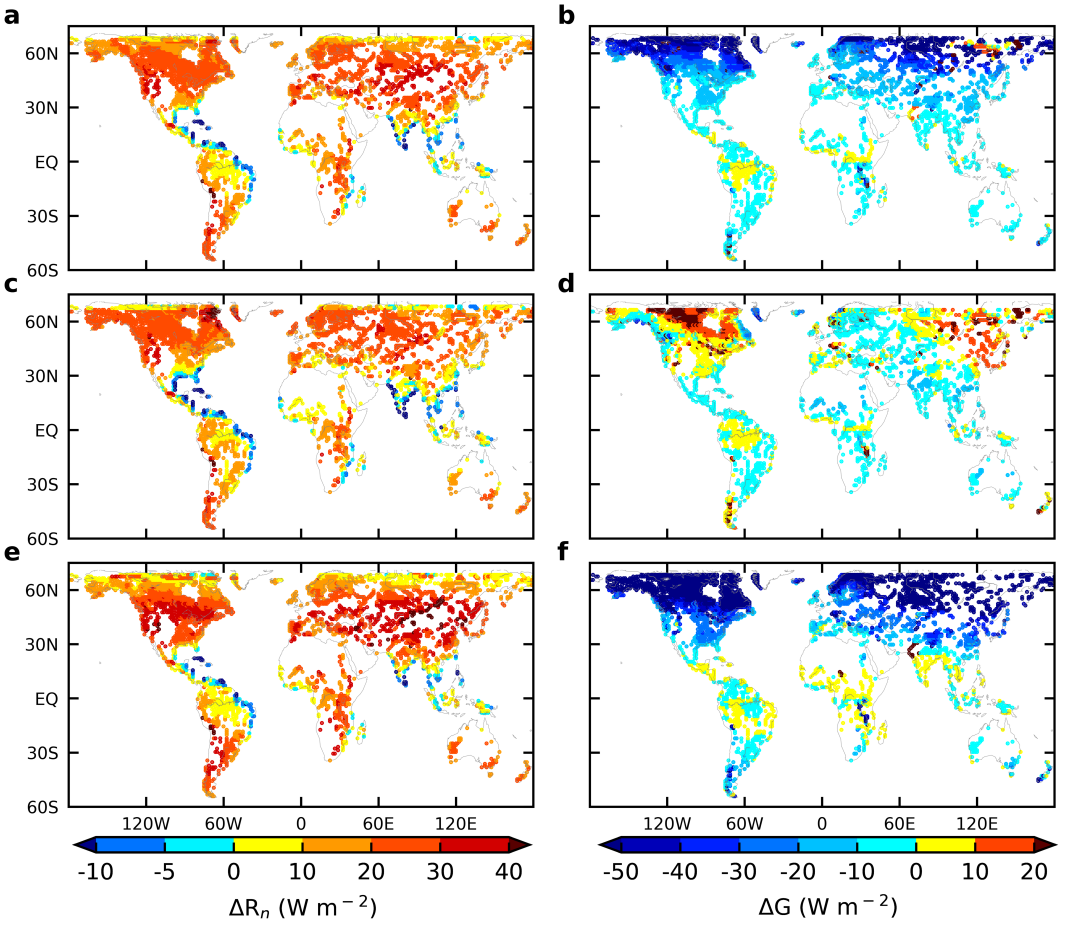

FIG. 5. Evaluating the difference in available energy ($R_n - G$). (a),(b) Entire period with open water. (c),(d) Summer. (e),(f) Autumn. (left) The spatial variability in the difference in R_n between the PM-ETA and LISSS simulations. (right) The spatial variability in the difference in water heat storage (G) between the ETA and the LISSS. Positive values denote overestimation by the PM-ETA compared to the LISSS and ETA.

of the PM-LISSS E for individual water bodies are nearly identical to those of the LISSS E (Table 1). Despite the very different model formulations, similar performance of the PM-LISSS and the LISSS demonstrates that the available energy ($R_n - G$) plays a dominant role in the PM E.

e. *Biases in PM-ETA E explained by biases in R_n and G*

The spatial distributions of the difference in R_n (and G) simulated by the PM-ETA and LISSS are shown in Fig. 5. The overestimated PM-ETA R_n and the underestimated G led to positive biases in the PM-ETA E. The global-mean PM-ETA R_n is 17% higher than the mean LISSS R_n (Fig. 5a). The overestimation of PM-ETA R_n is primarily due to the underestimation of outgoing longwave radiation by 25.9 W m^{-2} compared to the LISSS where the biases in incoming longwave radiation ($\Delta = -4.2$ W m^{-2}) and outgoing shortwave radiation ($\Delta = 2.3$ W m^{-2}) are substantially lower. Here, Δ represents the difference between the PM-ETA and LISSS estimates of net radiation. The global-mean PM-ETA G is 4.2 times smaller than that of the LISSS (Fig. 5b). The lowest biases in R_n and G occur in the tropical region followed by the temperate region. However, the biases in both R_n and G are higher for the cold and polar regions, which are consistent with the higher PM-ETA E biases for these regions (Fig. 2a). Assuming the effect of all other variables on PM-ETA E variability remains the same, the biases in the global-mean PM-ETA R_n and G explain about 54% of the higher PM-ETA E compared to the LISSS E. As discussed in section 2d, wind speed plays a minor role in E variability compared with the energy balance term at time scales longer than daily. The effect of wind speed on the overall uncertainty of the PM-ETA E is arguably secondary.

At seasonal time scales, the global-mean summer biases of the PM-ETA R_n and G are substantially lower than the global-mean autumn biases (Figs. 5c–f). In summer, the global-mean biases of the PM-ETA R_n and G are within ±19% and ±15%, respectively, for all study regions (Figs. 5c,d). The R_n and G biases remain nearly the same for the tropical region, while substantially higher for all other regions during autumn (Figs. 5e,f). Such seasonal distributions of the R_n and G biases are reflected in the corresponding E biases (Fig. 2). The higher available

energy ($R_n - G$) in the PM-ETA explains 82% and 52% higher PM E in summer and autumn, respectively, assuming the effect of all other variables on PM-ETA E variability remains unchanged.

The biases in the PM-ETA-simulated available energy trends from 2001 to 2016, as compared with the LISSS, explain the temporal PM-ETA E biases (Fig. 6). The largest biases of the PM-ETA available energy trends in the tropical, cold, and polar regions lead to the lowest correlation between the PM-ETA and LISSS E. Similar patterns of the temporal biases in the PM-ETA available energy and E are observed at seasonal time scales (Figs. 3b,c and 6b,c). For instance, the maximum biases in PM-ETA available energy trends occur in the polar region followed by the cold and tropical regions. Consequently, the corresponding biases of the PM-ETA E trends follow similar patterns for these regions. Our analysis confirms that the biases in the spatiotemporal variations of the PM-ETA E are primarily caused by those of R_n and G.

f. *Underlying mechanisms of biases in R_n and G simulated by the ETA*

While the ETA provides a practical framework for estimating lake E using the PM, it involves several assumptions to simplify diverse hydrological and climatic conditions. First, the ETA assumes a well-mixed water column (Edinger et al. 1968; Finch and Hall 2001) ignoring the effects of thermal stratification on surface energy fluxes, particularly during summer and autumn periods (Blanken et al. 2000; Boehrer and Schultze 2008; Hostetler and Bartlein 1990). In summer, the ETA tends to overestimate G (Fig. 5) by assuming the same warming rate of near-surface and deeper layers. Most of the energy from absorbed solar radiation in stratified lakes is confined to the upper layers with limited vertical mixing due to stable density gradients (Boehrer and Schultze 2008; Subin et al. 2012b). This simplified representation of water body thermal profile leads to positive bias in G estimates (Fig. 5d). In contrast, the ETA underestimates the release of heat from the deeper layers as the lakes cool and begin to destratify, leading to the negative G bias in autumn (Fig. 5f).

Second, the ETA does not account for sediment heat storage and its dynamic exchange with overlying water, which can significantly alter the surface energy fluxes. During warmer periods, lake sediments act as a heat sink, reducing the amount of energy available at the surface, while they release stored heat, buffering surface cooling in cooler months (Fang and Stefan 1996b; Stepanenko et al. 2013; Zdorovennova et al. 2021). Neglecting this two-way sediment–water heat flux leads to overestimates of R_n in ETA, particularly during autumn when lakes start to cool and sediment heat release becomes more pronounced (Fig. 5). This phenomenon also introduces bias in G because of an inaccurate representation of the thermal gradient between the surface and bottom layers. These biases in R_n and G lead to higher available energy and, consequently, higher E. This effect is most prominent in cold and polar regions, where seasonal stratification and sediment heat contributions play an increasingly important role, explaining the higher PM-ETA E bias (Fig. 2).

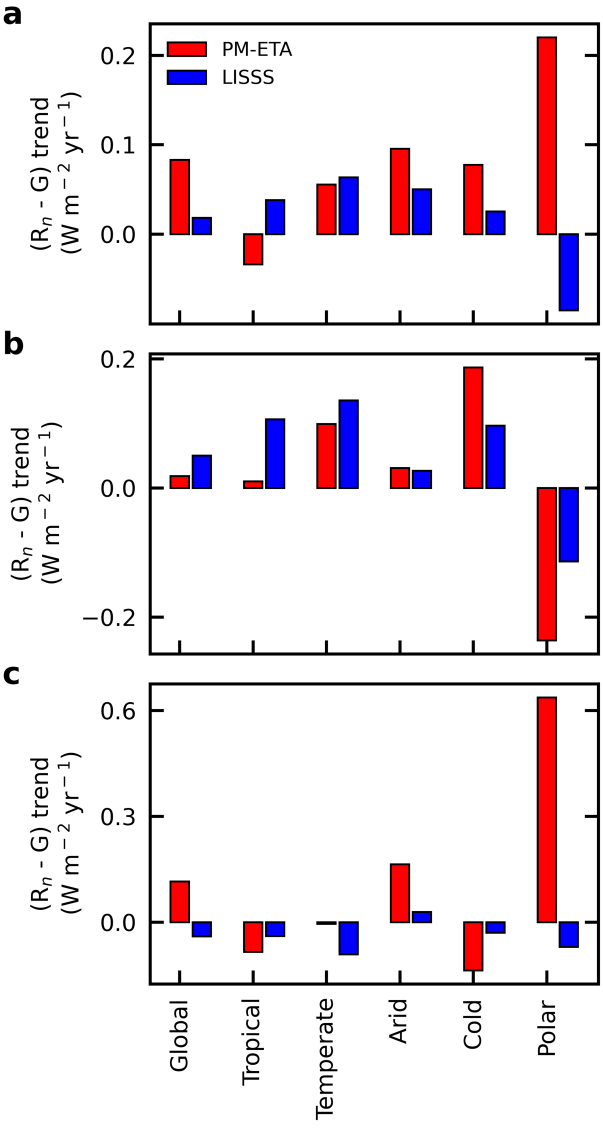

FIG. 6. Trends in the available energy ($R_n - G$). (a) The entire period with open water. (b) Summer. (c) Autumn.

Furthermore, ETA's assumption of open water conditions limits its accuracy in cold and polar regions, where lake energy budgets significantly alter during ice-covered periods (Hostetler and Bartlein 1990; Lei et al. 2011; Subin et al. 2012a). Although our study is limited to ice-free summer and autumn, it is important to recognize that lake ice tends to suppress direct E, increase surface albedo, and insulate lakes from atmospheric heat exchange, thereby reducing the energy available for E (Rouse 2000; Subin et al. 2012a). These effects are unaccounted for in the PM-ETA model and can introduce persistent biases in E estimates in cold and polar climates, particularly when atmospheric forcing data (e.g., air temperature and humidity) do not reflect the actual energy limitations associated with recent or preceding ice conditions. Both the physical simplifications of ETA and the omission of ice-related processes underscore the

need for the use of robust models like LISSS to simulate available energy and E from open water bodies.

g. *Implications of E biases for water resources*

The PM-ETA estimates 1630.1 km^3 of annual water loss through E from global water bodies with a total surface area of 2.32 million km^2 (~700 mm yr^{-1}). Although the E rate reaches its maximum at low latitudes (i.e., tropical, temperate, and arid regions) (Fig. 1), the highest accumulative E loss occurs in the cold region owing to the large number of water bodies (i.e., 49% of the total water bodies). It is estimated that the annual accumulative bias of the global-mean PM-ETA E is equivalent to 391.6 km^3 of water, which is about 84% of the water drawn from global reservoirs for municipal use during 2016 (FAO 2016). The large deviation of the PM-ETA E trends from the LISSS E trends suggests that caution should be exercised for water resource management and planning based on the PM-ETA E. Our analysis of the spatiotemporal PM-ETA E biases caused mainly by uncertainties of R_n and G data highlights the need of improving products of R_n and G, such as those provided by the LISSS, to improve the estimates of global lake E.

4. Conclusions

Our findings reveal a consistent overestimation of E by the PM-ETA on a global scale and across all study regions compared to both observations and the LISSS E. The largest positive biases of the PM-ETA E in the cold and polar regions, where R_n and G have pronounced seasonality, result from the overestimation of R_n and the underestimation of G by the ETA. Furthermore, the PM-ETA E trends deviate substantially from the LISSS E trends due to the biased trends of R_n and G. Using the LISSS-simulated R_n and G in the PM reduces the biases of the PM E to within ±5% on global scale and significantly improves the PM E for all regions across seasons. Our analysis highlights the need for improved data of R_n and G in the PM to drive the physical models of lake E and water resource management, especially in the context of a warming climate. It is important to emphasize that the biased estimates of R_n and G using ETA should not be interpreted as the weakness of the PM physics per se.

Acknowledgments. We acknowledge the support of the National Science Foundation (EAR-2002644, EAR-2006281, and EAR-2003076). U. F. was financially supported in part by the Government of Punjab in collaboration with the University of Agriculture, Faisalabad, Pakistan.

Data availability statement. The datasets that support the findings of this study and the code for the main figures are available as open access from Farooq et al. (2023).

REFERENCES

Bai, P., and Y. Wang, 2023: The importance of heat storage for estimating lake evaporation on different time scales: Insights from a large shallow subtropical lake. *Water Resour. Res.*, **59**, https://doi.org/10.1029/2023WR035123.

Beck, H. E., N. E. Zimmermann, T. R. McVicar, N. Vergopolan, A. Berg, and E. F. Wood, 2018: Present and future Köppen-Geiger climate classification maps at 1-km resolution. *Sci. Data*, **5**, 180214, https://doi.org/10.1038/sdata.2018.214.

Benyahya, L., D. Caissie, A. St-Hilaire, T. B. M. J. Ouarda, and B. Bobée, 2007: A review of statistical water temperature models. *Can. Water Resour. J.*, **32**, 179–192, https://doi.org/10.4296/cwrj3203179.

Blanken, P. D., and Coauthors, 2000: Eddy covariance measurements of evaporation from Great Slave Lake, northwest territories, Canada. *Water Resour. Res.*, **36**, 1069–1077, https://doi.org/10.1029/1999WR900338.

Boehrer, B., and M. Schultze, 2008: Stratification of lakes. *Rev. Geophys.*, **46**, RG2005, https://doi.org/10.1029/2006RG000210.

Bowen, I. S., 1926: The ratio of heat losses by conduction and by evaporation from any water surface. *Phys. Rev.*, **27**, 779–787, https://doi.org/10.1103/PhysRev.27.779.

Brutsaert, W., and H. Stricker, 1979: An advection-aridity approach to estimate actual regional evapotranspiration. *Water Resour. Res.*, **15**, 443–450, https://doi.org/10.1029/WR015i002p00443.

Caissie, D., 2006: The thermal regime of rivers: A review. *Freshwater Biol.*, **51**, 1389–1406, https://doi.org/10.1111/j.1365-2427.2006.01597.x.

Cui, Y., X. Zhang, and Y. Liu, 2021: Radiative and aerodynamic contribution to evaporation: Eddy-covariance comparison between a plain and a plateau lake. *Earth Space Sci.*, **8**, e2021EA001913, https://doi.org/10.1029/2021EA001913.

de Bruin, H. A. R., 1982: Temperature and energy balance of a water reservoir determined from standard weather data of a land station. *J. Hydrol.*, **59**, 261–274, https://doi.org/10.1016/0022-1694(82)90091-9.

——, and J. Q. Keijman, 1979: The Priestley-Taylor evaporation model applied to a large, shallow lake in the Netherlands. *J. Appl. Meteor.*, **18**, 898–903, https://doi.org/10.1175/1520-0450(1979)018<0898:TPTEMA>2.0.CO;2.

Downing, J. A., and Coauthors, 2006: The global abundance and size distribution of lakes, ponds, and impoundments. *Limnol. Oceanogr.*, **51**, 2388–2397, https://doi.org/10.4319/lo.2006.51.5.2388.

Du, X., N. K. Shrestha, D. L. Ficklin, and J. Wang, 2018: Incorporation of the equilibrium temperature approach in a soil and water assessment tool hydroclimatological stream temperature model. *Hydrol. Earth Syst. Sci.*, **22**, 2343–2357, https://doi.org/10.5194/hess-22-2343-2018.

——, G. Silwal, and M. Faramarzi, 2022: Investigating the impacts of glacier melt on stream temperature in a cold-region watershed: Coupling a glacier melt model with a hydrological model. *J. Hydrol.*, **605**, 127303, https://doi.org/10.1016/j.jhydrol.2021.127303.

Edinger, J. E., D. W. Duttweiler, and J. C. Geyer, 1968: The response of water temperatures to meteorological conditions. *Water Resour. Res.*, **4**, 1137–1143, https://doi.org/10.1029/WR004i005p01137.

Fang, X., and H. G. Stefan, 1996a: Long-term lake water temperature and ice cover simulations/measurements. *Cold Reg. Sci. Technol.*, **24**, 289–304, https://doi.org/10.1016/0165-232X(95)00019-8.

——, and ——, 1996b: Dynamics of heat exchange between sediment and water in a lake. *Water Resour. Res.*, **32**, 1719–1727, https://doi.org/10.1029/96WR00274.

FAO, 2016: AQUASTAT database. https://www.fao.org/nr/water/aquastat/data/query/index.html?lang=en.

Farooq, U., H. Liu, Q. Zhang, Y. Ma, J. Wang, and L. Shen, 2022: Spatial variability of global lake evaporation regulated

by vertical vapor pressure difference. *Environ. Res. Lett.*, **17**, 054006, https://doi.org/10.1088/1748-9326/ac614b.

——, ——, ——, J. Wang, and L. Shen, 2023: Global lake evaporation. Zenodo, https://doi.org/10.5281/zenodo.8201927.

Ficklin, D. L., Y. Luo, I. T. Stewart, and E. P. Maurer, 2012: Development and application of a hydroclimatological stream temperature model within the soil and water assessment tool. *Water Resour. Res.*, **48**, W01511, https://doi.org/10.1029/2011WR011256.

Finch, J. W., and R. L. Hall, 2001: Estimation of open water evaporation: A review of methods. R and D Tech. Rep. W6-043/TR, Environment Agency, 155 pp., https://assets.publishing.service.gov.uk/media/5a7b90d4e5274a7202e17ff6/sw6-043-tr-e-e.pdf.

Fraedrich, K., A. Behlau, G. Kerath, and G. Weber, 1977: A simple model for estimating the evaporation from a shallow water reservoir. *Tellus*, **29A**, 428–434, https://doi.org/10.3402/tellusa.v29i5.11375.

Gan, G., and Y. Liu, 2020: Heat storage effect on evaporation estimates of China's largest freshwater lake. *J. Geophys. Res. Atmos.*, **125**, e2019JD032334, https://doi.org/10.1029/2019JD032334.

Guan, X., C. Liu, J. Zhang, G. Wang, Z. Bao, and J. Jin, 2022: On the attribution of changing water surface evaporation across China. *J. Hydrol.*, **40**, 100991, https://doi.org/10.1016/j.ejrh.2022.100991.

Hamdani, I., S. Assouline, J. Tanny, I. M. Lensky, I. Gertman, Z. Mor, and N. G. Lensky, 2018: Seasonal and diurnal evaporation from a deep hypersaline lake: The dead sea as a case study. *J. Hydrol.*, **562**, 155–167, https://doi.org/10.1016/j.jhydrol.2018.04.057.

Harbeck, G. E., M. A. Kohler, and G. E. Koberg, 1958: Water-loss investigations: Lake Mead studies. Geological Survey Professional Paper 298, US Geological Survey, 111 pp., https://pubs.usgs.gov/pp/0298/report.pdf.

Hebert, C., D. Caissie, M. G. Satish, and N. El-Jabi, 2011: Study of stream temperature dynamics and corresponding heat fluxes within Miramichi River catchments (New Brunswick, Canada). *Hydrol. Processes*, **25**, 2439–2455, https://doi.org/10.1002/hyp.8021.

Hostetler, S. W., and P. J. Bartlein, 1990: Simulation of lake evaporation with application to modeling lake level variations of Harney-Malheur Lake, Oregon. *Water Resour. Res.*, **26**, 2603–2612, https://doi.org/10.1029/WR026i010p02603.

Hu, C., Y. Wang, W. Wang, S. Liu, M. Piao, W. Xiao, and X. Lee, 2017: Trends in evaporation of a large subtropical lake. *Theor. Appl. Climatol.*, **129**, 159–170, https://doi.org/10.1007/s00704-016-1768-z.

Keijman, J. Q., 1974: The estimation of the energy balance of a lake from simple weather data. *Bound.-Layer Meteor.*, **7**, 399–407, https://doi.org/10.1007/BF00240841.

Korver, M. C., B. Lehner, J. A. Cardille, and L. Carrea, 2024: Surface water temperature observations and ice phenology estimations for 1.4 million lakes globally. *Remote Sens. Environ.*, **308**, 114164, https://doi.org/10.1016/j.rse.2024.114164.

Kourzeneva, E., H. Asensio, E. Martin, and S. Faroux, 2012: Global gridded dataset of lake coverage and lake depth for use in numerical weather prediction and climate modelling. *Tellus*, **64A**, 15640, https://doi.org/10.3402/tellusa.v64i0.15640.

Kummu, M., and Coauthors, 2016: The world's road to water scarcity: Shortage and stress in the 20th century and pathways towards sustainability. *Sci. Rep.*, **6**, 38495, https://doi.org/10.1038/srep38495.

La Fuente, S., E. Jennings, J. D. Lenters, P. Verburg, Z. Tan, M. Perroud, A. B. Janssen, and R. I. Woolway, 2024: Ensemble modeling of global lake evaporation under climate change. *J. Hydrol.*, **631**, 130647, https://doi.org/10.1016/j.jhydrol.2024.130647.

Layden, A., C. Merchant, and S. MacCallum, 2015: Global climatology of surface water temperatures of large lakes by remote sensing. *Int. J. Climatol.*, **35**, 4464–4479, https://doi.org/10.1002/joc.4299.

Lehner, B., and P. Döll, 2004: Development and validation of a global database of lakes, reservoirs and wetlands. *J. Hydrol.*, **296**, 1–22, https://doi.org/10.1016/j.jhydrol.2004.03.028.

Lei, R., M. Leppäranta, A. Erm, E. Jaatinen, and O. Pärn, 2011: Field investigations of apparent optical properties of ice cover in finnish and Estonian lakes in winter 2009. *Est. J. Earth Sci.*, **60**, 50–64, https://doi.org/10.3176/earth.2011.1.05.

Lenters, J. D., T. K. Kratz, and C. J. Bowser, 2005: Effects of climate variability on lake evaporation: Results from a long-term energy budget study of Sparkling Lake, northern Wisconsin (USA). *J. Hydrol.*, **308**, 168–195, https://doi.org/10.1016/j.jhydrol.2004.10.028.

Lieberherr, G., and S. Wunderle, 2018: Lake surface water temperature derived from 35 years of AVHRR sensor data for European Lakes. *Remote Sens.*, **10**, 990, https://doi.org/10.3390/rs10070990.

Liu, H., Q. Zhang, and G. Dowler, 2012: Environmental controls on the surface energy budget over a large southern inland water in the United States: An analysis of one-year eddy covariance flux data. *J. Hydrometeor.*, **13**, 1893–1910, https://doi.org/10.1175/JHM-D-12-020.1.

McJannet, D. L., I. T. Webster, and F. J. Cook, 2012: An area-dependent wind function for estimating open water evaporation using land-based meteorological data. *Environ. Modell. Software*, **31**, 76–83, https://doi.org/10.1016/j.envsoft.2011.11.017.

McMahon, T. A., M. C. Peel, L. Lowe, R. Srikanthan, and T. R. McVicar, 2013: Estimating actual, potential, reference crop and pan evaporation using standard meteorological data: A pragmatic synthesis. *Hydrol. Earth Syst. Sci.*, **17**, 1331–1363, https://doi.org/10.5194/hess-17-1331-2013.

Mekonnen, M. M., and A. Y. Hoekstra, 2016: Four billion people facing severe water scarcity. *Sci. Adv.*, **2**, e1500323, https://doi.org/10.1126/sciadv.1500323.

Moreo, M. T., 2015: Evaporation data from Lakes Mead and Mohave, Nevada and Arizona, March 2010 through April 2015. https://doi.org/10.5066/F79C6VG3.

Muzammil, M., A. Zahid, U. Farooq, N. Saddique, and L. Breuer, 2023: Climate change adaptation strategies for sustainable water management in the Indus basin of Pakistan. *Sci. Total Environ.*, **878**, 163143, https://doi.org/10.1016/j.scitotenv.2023.163143.

Oleson, K. W., and Coauthors, 2013: Technical description of version 4.5 of the Community Land Model (CLM). NCAR Tech. Note NCAR/TN-503+STR, UCAR/NCAR, 434 pp., https://opensky.ucar.edu/islandora/object/%3A3830.

Pasquill, F., 1943: Evaporation from a plane, free-liquid surface into a turbulent air stream. *Proc. Roy. Soc. London*, **182A**, 75–95, https://doi.org/10.1098/rspa.1943.0024.

Pastorello, G., and Coauthors, 2020: The FLUXNET2015 dataset and the ONEFlux processing pipeline for eddy covariance data. *Sci. Data*, **7**, 225, https://doi.org/10.1038/s41597-021-00851-9.

Penman, H. L., 1948: Natural evaporation from open water, bare soil and grass. *Proc. Roy. Soc. London*, **193A**, 120–145, https://doi.org/10.1098/rspa.1948.0037.

Piccolroaz, S., and Coauthors, 2024: Lake water temperature modeling in an era of climate change: Data sources, models,

and future prospects. *Rev. Geophys.*, **62**, e2023RG000816, https://doi.org/10.1029/2023RG000816.

Priestley, C. H. B., and R. J. Taylor, 1972: On the assessment of surface heat flux and evaporation using large-scale parameters. *Mon. Wea. Rev.*, **100**, 81–92, https://doi.org/10.1175/1520-0493(1972)100<0081:OTAOSH>2.3.CO;2.

Prigent, C., F. Papa, F. Aires, C. Jimenez, W. B. Rossow, and E. Matthews, 2012: Changes in land surface water dynamics since the 1990s and relation to population pressure. *Geophys. Res. Lett.*, **39**, L08403, https://doi.org/10.1029/2012GL051276.

Roderick, M. L., L. D. Rotstayn, G. D. Farquhar, and M. T. Hobbins, 2007: On the attribution of changing pan evaporation. *Geophys. Res. Lett.*, **34**, L17403, https://doi.org/10.1029/2007GL031166.

Rouse, W. R., 2000: The energy and water balance of high-latitude wetlands: Controls and extrapolation. *Global Change Biol.*, **6**, 59–68, https://doi.org/10.1046/j.1365-2486.2000.06013.x.

Sen, P. K., 1968: Estimates of the regression coefficient based on Kendall's tau. *J. Amer. Stat. Assoc.*, **63**, 1379–1389, https://doi.org/10.1080/01621459.1968.10480934.

Shao, C., J. Chen, H. Chu, C. A. Stepien, and Z. Ouyang, 2020: Intra-annual and interannual dynamics of evaporation over western Lake Erie. *Earth Space Sci.*, **7**, e2020EA001091, https://doi.org/10.1029/2020EA001091.

Sheffield, J., G. Goteti, and E. F. Wood, 2006: Development of a 50-year high-resolution global dataset of meteorological forcings for land surface modeling. *J. Climate*, **19**, 3088–3111, https://doi.org/10.1175/JCLI3790.1.

Stepanenko, V. M., and Coauthors, 2013: A one-dimensional model intercomparison study of thermal regime of a shallow, turbid midlatitude lake. *Geosci. Model Dev.*, **6**, 1337–1352, https://doi.org/10.5194/gmd-6-1337-2013.

Stewart, R. B., and W. R. Rouse, 1976: A simple method for determining the evaporation from shallow lakes and ponds. *Water Resour. Res.*, **12**, 623–628, https://doi.org/10.1029/WR012i004p00623.

Subin, Z. M., L. N. Murphy, F. Li, C. Bonfils, and W. J. Riley, 2012a: Boreal lakes moderate seasonal and diurnal temperature variation and perturb atmospheric circulation: Analyses in the Community Earth System Model 1 (CESM1). *Tellus*, **64A**, 15639, https://doi.org/10.3402/tellusa.v64i0.15639.

——, W. J. Riley, and D. Mironov, 2012b: An improved lake model for climate simulations: Model structure, evaluation, and sensitivity analyses in CESM1. *J. Adv. Model. Earth Syst.*, **4**, M02001, https://doi.org/10.1029/2011MS000072.

Tian, W., X. Liu, K. Wang, P. Bai, C. Liu, and X. Liang, 2022: Estimation of global reservoir evaporation losses. *J. Hydrol.*, **607**, 127524, https://doi.org/10.1016/j.jhydrol.2022.127524.

Wang, W., X. Lee, W. Xiao, S. Liu, N. Schultz, Y. Wang, M. Zhang, and L. Zhao, 2018: Global lake evaporation accelerated by changes in surface energy allocation in a warmer climate. *Nat. Geosci.*, **11**, 410–414, https://doi.org/10.1038/s41561-018-0114-8.

Xiao, K., and Coauthors, 2018: Evaporation from a temperate closed-basin lake and its impact on present, past, and future water level. *J. Hydrol.*, **561**, 59–75, https://doi.org/10.1016/j.jhydrol.2018.03.059.

Xie, H., X. Zhu, and D.-Y. Yuan, 2015: Pan evaporation modelling and changing attribution analysis on the Tibetan Plateau (1970–2012). *Hydrol. Procesess*, **29**, 2164–2177, https://doi.org/10.1002/hyp.10356.

You, G., Y. Zhang, Y. Liu, Q. Song, Z. Lu, Z. Tan, C. Wu, and Y. Xie, 2013: On the attribution of changing pan evaporation in a nature reserve in SW China. *Hydrol. Processess*, **27**, 2676–2682, https://doi.org/10.1002/hyp.9394.

Zdorovennova, G., A. Terzhevik, N. Palshin, T. Efremova, S. Bogdanov, and R. Zdorovennov, 2021: Seasonal change in heat flux at the water-bottom sediment boundary in a small lake. *J. Phys: Conf. Ser.*, **2131**, 032080, https://doi.org/10.1088/1742-6596/2131/3/032080.

Zhang, Z., and Coauthors, 2020: A dataset of microclimate and radiation and energy fluxes from the Lake Taihu eddy flux network. *Earth Syst. Sci. Data*, **12**, 2635–2645, https://doi.org/10.5194/essd-12-2635-2020.

Zhou, W., L. Wang, D. Li, and L. R. Leung, 2021: Spatial pattern of lake evaporation increases under global warming linked to regional hydroclimate change. *Commun. Earth Environ.*, **2**, 255, https://doi.org/10.1038/s43247-021-00327-z.

Zhu, S., X. Du, and W. Luo, 2019: Incorporation of the simplified equilibrium temperature approach in a hydrodynamic and water quality model – CE-QUAL-W2. *Water Supply*, **19**, 156–164, https://doi.org/10.2166/ws.2018.063.